INTERNATIONAL JOURNAL OF AUTOMOTIVE AND MECHANICAL ENGINEERING
ISSN: 2229-8649 e-ISSN: 2180-1606
VOLUME 23, ISSUE 2, 2026, 13488 - 13503
DOI: https://doi.org/10.15282/ijame.23.2.2026.2.1021

RESEARCH ARTICLE

Experimental analysis of aerodynamic performance in simplified ground vehicle prototypes

Mohammed Kh. Abbas

Department of Mechanical Engineering, College of Engineering, University of Diyala, Diyala, Iraq ,32001

Abstract - Aerodynamic drag reduction and flow control remain major challenges in improving vehicle fuel efficiency, high-speed stability, and overall aerodynamic performance of ground vehicles. Flow separation and wake formation behind vehicle bodies significantly influence drag generation, especially for simplified vehicle geometries. Therefore, this study experimentally investigates the aerodynamic performance of three simplified ground vehicle models tested in a subsonic open-circuit wind tunnel. A Suzuki Vitara (Car 1) that is 6.67% smaller and a Lamborghini Aventador (Car 2) that is 5% smaller are two of the models. The third model (Car 3) has a new aerodynamic design that is based on the shape of a fastback. The Reynolds numbers (Re) of the cars that were tested were between 1.5×10^5 and 6.0×10^5, which is the same as wind speeds of 10 to 30 m/s. We employed a calibrated hot-wire anemometer and digital manometer to measure the local velocity, the distribution of the surface pressure coefficient, and the aerodynamic forces. Car 3 always had the lowest drag coefficient, with a minimum C_D of 0.242, which is 29% lower than Car 1 and 2% lower than Car 2. Adding a rear wing to Car 3 cut lift by up to 25% at high Re, but only added a modest amount of drag ($\Delta C_D = +0.006$). Based on numerous trials and device calibration, the maximum measurement errors for drag were ± 1.4 % and for lift were ± 1.3 %. The findings elucidate that the shape of the back and the use of aerodynamic devices can significantly impact the wake development, drag reduction, and stability enhancement.

Article History
Received : 26 June 2025
Revised : 29 January 2026
Accepted : 12 May 2026
Published : 30 June 2026

Keywords
Aerodynamic performance
Drag coefficient
Ground vehicle prototypes
Wind tunnel testing

1. Introduction

The development of low-drag aerodynamic designs for automobiles has long been an objective of manufacturers seeking to boost fuel economy, limit emissions, and improve stability at high speeds. Aerodynamic drag is the principal resistance to motion at both moderate and high velocities; thus, small changes to a vehicle's geometric form can result in large gains in overall aerodynamic drag and fuel efficiency. Relevant studies have specified the three principal mechanisms impacting drag development as follows: flow separation, the wake structure generated behind a vehicle and the design of the rear-end [1] [2], [3]. The three aforementioned aerodynamic mechanisms have been extensively investigated using both simplified benchmark models and production-type geometries. Flow separation and wake generation have both been studied utilising the Ahmed body benchmark. This, in turn, permits scholars to reveal how various rear-end geometries would impact pressure drag [4], [5], [6], [7].

Previous investigations conducted on scale models of sports utility vehicle (SUVs) and passenger cars have depicted that aerodynamic drag is precisely sensitive to the rear end form of automobiles, and both wind tunnel and computational flow simulations have acknowledged the presence of low-pressure wake zones, and that using a suitable trailing edge design can mitigate the size of these low-pressure wake zones. In recent times, several studies have been conducted on hybrid and high-performance automobiles utilising wind tunnel testing and computational flow modelling techniques to investigate the aerodynamic features of these vehicles. These investigations established that by using suitable streamlined designs, aerodynamic drag can be significantly reduced while overall efficiency can be enhanced. These contributions emphasise the importance of geometric refinement in altering the aerodynamic features of road vehicles [8], [9], [10], [11] [12], [13].

Flow separation around the vehicle structure accounts for more than 50% of the overall aerodynamic drag on ground vehicles. Much of the air flow around cars is three dimensional with enormous separation zones, unique vortices and complex recirculation regions[14] ,[15], [16] Flow visualisation techniques are vital for understanding and reducing flow separation and drag. But other experts say these methods alone aren't enough because they don't show all that happens in the actual world. Also, really doing things and testing them out in real life in different places can provide you some crucial knowledge that you can't get from simulations. Research has shown that installing ducting components into the Ahmed body, a regularly used reduced vehicle model, can result in a reduction of 15% in aerodynamic drag [6]. It was also known that the main reason road cars experienced aerodynamic drag was pressure drag due to flow separation at the back of the body. D. Dhande and M. Bauskar [2] used a 1:32 scale model of a sports utility vehicle (SUV) in a subsonic wind tunnel to show that a well-optimised aerodynamic shape may considerably reduce drag force (F_D) and drag coefficient (C_D). The results were very similar to those of Fluent and Gambit, two programs used for Computational Fluid Dynamics (CFD). Also, the vehicle's rear geometry has a big effect on how aerodynamic it is since flow separation at the back creates low-

*CORRESPONDING AUTHOR | **Mohammed Kh. Abbas** | ✉ mohammedkhudhair_eng@uodiyala.edu.iq

pressure wake zones [4]. Furthermore, computer models reveal that low-pressure areas usually arise at the back borders, whereas high-pressure areas are found near the front grille and windscreen.

Even though there have been decent developments with the way cars move through the air, there are still no organized experiments looking at how well various kinds of production style cars would contrast with the aerodynamics of recently designed conceptual cars in a controlled wind tunnel environment. Specifically, there is not much empirical data on how changes to the shape of the vehicle can influence the drag and the lift, with the use of scaled-to-1/4 size physical models for different Reynolds number conditions via experiments performed in the wind tunnel. To fill this gap in the open literature, this study would use three models of vehicles generated by 3D printing technology: two existing models, commercial vehicle designs, and one newly designed aerodynamic concept vehicle. The findings of testing each vehicle will be measured by drag, lift, pressure distribution, and local velocity features, and testing will be achieved to specify the influence of adding a rear wing on the aerodynamic characteristics of the conceptual model vehicle.

This work provides a targeted experimental dataset for the three specifically fabricated models (a Vitara-derived shape, an Aventador-derived shape, and a novel fastback Car-3) tested over Re from 1.5×105 to 6.0×105. It includes the first reported wind-tunnel measurements demonstrating the Reynolds-dependent trade-off between rear-wing-induced downforce and drag penalty for the new Car-3 geometry under the present mounting and blockage conditions. The dataset also incorporates a complete uncertainty budget and blockage-corrected aerodynamic coefficients, offering reliable input for future CFD benchmarking and small-scale wind-tunnel test planning. Therefore, the main objective of this study is to experimentally evaluate and compare the aerodynamic performance of three simplified ground vehicle models under different Reynolds numbers using wind-tunnel testing, with particular emphasis on drag reduction, lift behaviour, pressure distribution, and the aerodynamic influence of a rear wing on the proposed fastback configuration.

2. Materials and Methods

The open-loop wind tunnel (WT) in the Mechanical Engineering Laboratory at UOD-COE (Figure 1) was used for the aerodynamic tests. The tunnel has a bell mouth with an air straightener, a settling chamber, a contraction cone, a clear acrylic test section, and a diffuser. All specifications of the UOD-COE wind tunnel are listed in Table 1. Before using the system, the equipment was carefully levelled to ensure it was level. The airflow was created using a variable-speed motor that could go from 0 to 30 m/s, which is about the same as a Reynolds number of 7×10^5. The tunnel is made of plastic that has fibres, and the smooth walls of the test portion reduce the impact of surface roughness on the model scale. The test section is 0.32 × 0.32 × 0.53 m in size. The blockage ratio in the test area was less than 5%, which is usually considered fine for subsonic vehicle testing. A 25 cm × 0.5 cm slot was cut into the upper wall of the test portion. Three vehicle models were fabricated using a Creality K1 Max 3D printer, as shown in Figure 2.

i. Car 1: Suzuki Vitara JX 3-door Hard Top model, scale 1:15
ii. Car 2: Lamborghini Aventador LP 750-4 model, scale 1:20
iii. Car 3: New aerodynamic design (modified from Car 2), scale 1:20

All models were solid, smooth-surfaced, and mounted on the tunnel floor, fixed from above using a threaded rod to prevent vibration. The vehicle models were mounted directly on the wind-tunnel floor. A moving ground belt or boundary-layer suction system was not available in the present facility. Therefore, the ground condition corresponds to a stationary floor configuration, which is commonly adopted in small-scale subsonic wind-tunnel testing. Twelve pressure and velocity measurement locations were distributed along the upper centerline of each model. A fixed copper needle was used to place the pressure taps 0.5 mm above the surface, not inside the body. (Figure 3) shows the schematic diagram for Car 3, with the 12 probe sites plotted on the car's geometry. Additional upstream (point 1) and downstream (point 14) positions were used for wake measurements. In the same arrangement, Cars 1 and 2 are mounted on the tunnel floor.

The blockage ratios for Car 1, Car 2, and Car 3 were 9%, 4.68%, and 4.62%, respectively. Only Car 1 was slightly above the ideal 7.5% limit; however, blockage correction factors were applied following standard methodologies. All characteristics of the car model are listed in Table 2. Although the vehicle models were manufactured at different geometric scales (1:15 for Car 1 and 1:20 for Cars 2 and 3), all aerodynamic measurements and comparisons were performed using non-dimensional coefficients, namely the drag coefficient (C_D), lift coefficient (C_l) and pressure coefficient (Cp). Blockage correction factors were applied individually for each model to account for differences in frontal area and blockage ratio.

This access allowed for the measurement of velocity and pressure at 14 stations: point 1 upstream, 12 points above the upper surface, and point 14 downstream. The model was placed directly on the floor of the test portion and held in place from above, which is how the tunnel was built. A Testo 425 hot-wire anemometer Figure 4(a) with a precision of ±0.03 m/s was used to measure air velocity, and an AHJ-501 digital manometer Figure 4(b) with an accuracy of ±0.3% FSO and a resolution of 10 Pa was used to measure static pressure. The flow entering the test portion had a consistent velocity profile with variations of less than ±1.5%. The hot wire and manometer detected turbulence-intensity levels of 6.7% and 5.6%, respectively. Corrections were made to the measurements to make up for the uncertainty in freestream velocity and static pressure. To achieve accurate results, readings were obtained repeatedly at different times and averaged in a controlled-temperature environment. The hot-wire probe worked slightly outside of its calibration range, but the resulting uncertainty (0–0.15 m/s) was still acceptable. At greater speeds, the uncertainty stayed below 2%. Table 3 shows all of the specifications for the instruments.

Because of the way the tunnel was built, it was not possible to access the area below the model without changing the mounting or harming the tunnel structure. Due to wind-tunnel mounting constraints, pressure measurements were conducted exclusively on the upper surface of the vehicle models. Access to the underbody region was not feasible without

modifying the tunnel floor or the model support system. As a result, the pressure distribution was only measured on the top surface. The measurements we have are good enough to describe the flow above the model and look at the aerodynamic trends that were studied in this study, but full pressure integration over both surfaces is best. Due to facility limitations, Particle Image Velocimetry (PIV) and smoke or tuft flow visualization techniques were not available during the present experimental campaign. Car 3 was developed from the modified fastback configuration derived from the baseline geometry of Car 2. Changes in the geometric shape of the vehicle are: a new rear-slope angle, smoothing of the roof transition to deck, and enhanced rear-end shape for a better pressure recovery within the vehicle's wake. These variations were made to aid control flow separation and develop a more stable structure of the vehicle's wake while maintaining similar features to the original vehicle.

To guarantee all external dimensions of Car 3 could be duplicated, a parametric CAD model was developed to describe these dimensions. The finished parts were then built using fused deposition modeling (FDM). Using precision measurements, the geometric differences between the CAD and the 3D printed models were measured, and all dimensional differences were maintained under 0.7%. A comprehensive comparison between the nominal CAD dimensions and the fabricated models, including manufacturing tolerances, is provided in Table 4.

Figure 1. UOD-COE wind tunnel

Table 1. Specifications of the UOD-COE wind tunnel

Type	Open wind tunnel
Duct material	Fiber-reinforced plastic
Speed variation	10% to 100% (controlled via a frequency drive controller)
Test section material	Acrylic sheet (10 mm thickness)
Blower Fan	8 blades
Motor	AC motor, 3480 RPM, 12 HP
Air Length	4.58 m
Turbulence intensity	0.05

Car1 Car 2 Car 3

Figure 2. 3-D-printed car models were used for the experimental tests

Car 3 has a different rear-body shape than Car 2, with a new rear-slope profile and a rear wing added. However, it has the same overall size and front area. These changes were made to improve rear-end pressure recovery and reduce wake-induced drag.

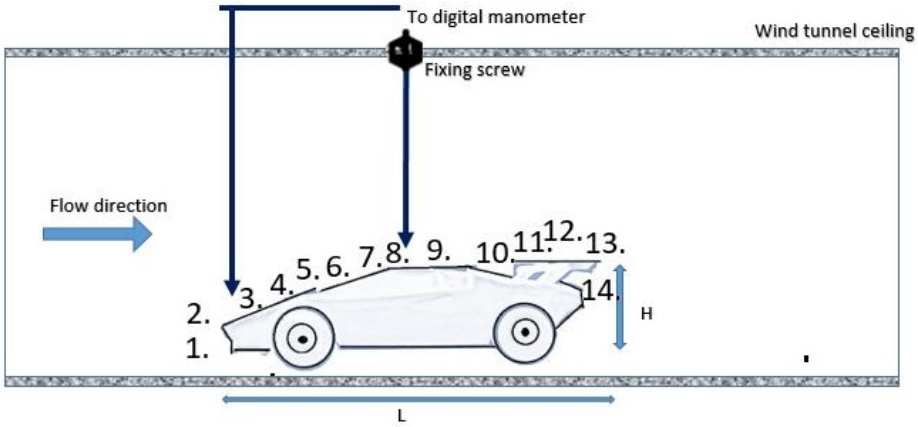

Figure 3. Schematic of the Car 3 model in the wind-tunnel test section

Table 2: Characteristics of the car model

	Car1	Car 2	Car 3
Scale	1/15	1/20	1/20
Total Length (L) mm	254	241.75	229
Total width without mirrors (W) mm	113	101.5	102
Total height (H) mm	112.67	56.8	56.75
Frontal area Af, m2	0.009225	0.00479	0.004735
Blockage ratio B, %	9	4.68	4.62
Material of models	plastic	plastic	Plastic
Rear wing dimensions, mm	-	-	Height=30 Width=5 Long =68

(a) (b)

Figure 4. (a) Hot-wire anemometer and (b) digital manometer

Table 3. Specifications of all instruments used in the study

Device	Specification	value
Hot wire (Testo 425)	Measuring ranges	Velocity: 0.1–30 m/s; Temperature: –20 to +70°C
	Resolutions	0.01 m/s (velocity); 0.1 °C (temperature)
	Accuracies	Velocity: ± (0.03 m/s + 4% mv) [0.01–20 m/s]; ± (0.5 m/s + 5% mv) [20.01–30 m/s] — Temp: ±0.5°C (0–60°C)
	Calibration Reference	Factory calibration using ISO-traceable air-flow and temperature standards
Digital manometer (AHJ-501)	Measuring ranges	± 2.999 psi
	Resolutions	± 0.006 psi (±0.2% FSO)
	Accuracies	± 0.3% FSO at 25°C
	Calibration Reference	Factory calibration against traceable pressure standard at 25°C (FSO-based)

2.1. Measurement Devices and Calibration

2.1.1 Hot-wire anemometer

A Testo 425 hot-wire anemometer was used to measure local velocity. Calibration was performed using an ISO-traceable low-speed airflow standard. A multi-point calibration curve (0–20 m/s) was generated, with extrapolation error at higher speeds verified to remain below 2%. Zero-offset compensation was performed before each test.

2.1.2 Digital Manometer

Static pressure was measured using an AHJ-501 digital manometer (accuracy ±0.3% FSO). Calibration included:

i. Zero reference calibration at ambient pressure
ii. Cross-checking with a U-tube water manometer
iii. Hysteresis and drift verification

2.1.3 Geometric Deviations and Manufacturing Tolerances.

Geometric deviations are discrepancies between the CAD model and the actual 3D-printed prototype that are caused by constraints in the manufacturing process. Manufacturing tolerances set the limits on what is acceptable and ensure everything works right. Table 4 compares the key external dimensions of the CAD model and the 3D-printed wind-tunnel model. Geometric deviations between the CAD model and the 3D-printed prototypes were measured with a Vernier calliper (± 0.02 mm). The maximum dimensional deviation was less than 0.7%. Average surface roughness of the FDM-printed models was Ra ≈ 11–14 µm.

Table 4. Geometric deviations between the CAD and 3D-printed car models

Car	Parameter	CAD (mm)	Printed Model (mm)	Deviation (mm)	% Error
Car 1	length	254.00	253.3	-0.70	0.28 %
	width	113.00	112.4	-0.60	0.53 %
	height	112.67	112.2	-0.47	0.42 %
Car 2	length	241.75	241.1	-0.65	0.27 %
	width	101.50	100.9	-0.60	0.59 %
	height	56.80	56.55	-0.25	0.44 %
Car 3	length	229.00	228.4	-0.60	0.26 %
	width	102.00	101.3	-0.70	0.69 %
	height	56.75	56.60	-0.15	0.26 %

2.1.4 Uncertainty Analysis

Uncertainty propagation for lift and drag coefficients included contributions from[17], [18], [19], [20]:

i. Velocity measurement (±0.03 m/s + 4% reading)
ii. Pressure resolution (10 Pa)
iii. Probe positioning (±0.5 mm)
iv. Blockage correction uncertainty

These manufacturing aspects, together with instrument uncertainty and blockage corrections, were incorporated into a full experimental uncertainty analysis. The measurement, geometric, roughness, and blockage contributions were combined using root-sum-square (RSS) propagation. For the two low-blockage models (Car 2 and Car 3, B ≈ 4.6–4.7%), the combined uncertainty is ±2.78% for $C_D$and ± 2.30% for C_L . For Car 1, which has a higher blockage ratio (B = 9%), a conservative blockage-correction uncertainty was included, resulting in combined uncertainties of ± 3.71% for $C_D$and ± 2.60% for C_L. Absolute uncertainties for each reported coefficient are given alongside the coefficient values in Table 5.

Table 5. Measurement devices, calibration procedures, and associated uncertainty contributions

Device	Measured quantity	Measurement range	Accuracy	Calibration method	Uncertainty contribution
Hot wire anemometer (Testo 425)	Local velocity	0–30 m/s	± 0.03 m/s + 4%	ISO-traceable low-speed airflow standard	Velocity uncertainty
Digital manometer (AHJ-501)	Static pressure	± 2000 Pa	± 0.3% FSO	Zero-reference + U-tube cross-check	Pressure uncertainty
Probe positioning system	Probe location	-	± 0.5 mm	Manual alignment and repeatability check	Positioning uncertainty
Wind tunnel blockage correction	Drag correction	-	-	Standard blockage correction method	Blockage uncertainty
Combined uncertainty	Cd, Cl	-	-	Error propagation method	Car 2 and 3: (Cd: ± 2.78%, Cl: ± 2.3%) and Car 1(Cd: ± 3.71%, Cl: ±2.6%)

The reported uncertainties for C_D and C_l include contributions from measurement accuracy, blockage correction, probe positioning, and geometric deviations between the CAD and printed models, which are discussed in the next section.

2.2. Experimental Methodology Calculation

To calculate lift and drag coefficients and lift and drag forces, the upstream (point 1) and downstream (point 14) velocities, which are shown at the point before and behind the car model, were recorded using a hot-wire instrument. Additionally, the static pressure and pressure coefficient in these areas were measured using a digital manometer. Twelve locations above the vehicle's surface centerline were also used to record velocity and static pressure. Equation 1 is used to compute an actual drag force.[21], [22], [23]

$$F_{d_{act}} = 0.5\ \rho\ A_f\left(V^2_{upstream} - V^2_{downstream}\right) \tag{1}$$

In this equation, V_{up} represents the upstream velocity, $V_{downstream}$ denotes the downstream velocity, A_f is the frontal area of the scale model, and ρ indicates the density of air.

The theoretical drag force is calculated using upstream velocity only, as given by Equation 2 [23].[24]

$$F_{d_{the}} = 0.5\ \rho\ A_f\left(V^2_{upstream}\right) \tag{2}$$

The ratio of actual drag force to the theoretical drag force is represented by the drag coefficient (C_D) [9].

$$C_d = \frac{F_{d_{act}}}{F_{d_{the}}} \tag{3}$$

The blockage ratio measures the degree to which the vehicle obstructs airflow in the wind tunnel. One of the most crucial elements influencing the precision of aerodynamic measurements is the blockage ratio, as stated in Equation 4, and it is recommended to be less than 7.5% in wind tunnel testing [23].

$$B = \frac{A_f}{A_w} \tag{4}$$

A_w is the area of the wind tunnel section.

The pressure coefficient of the flow on car surfaces is defined in Equation 5 [25].

$$Cp_{,i} = \frac{P_i - P_\infty}{q} \tag{5}$$

In this equation, P_i represents the local surface pressure, and P_∞ static denotes the far-field static pressure. Reynolds number is defined in Equation 6[26] [27].

$$Re = \frac{\rho\ V\ L}{\mu} \tag{6}$$

L is the characteristic vehicle length and μ is the dynamic viscosity of the air. The dynamic pressure (q) can be calculated using Equation 7[23] .

$$q = 0.5\ \rho V^2_{upstream} \tag{7}$$

The lift force F_L can be estimated using this formula [20], [23].

$$F_L = \sum_{i=1}^{N} (\ P_i - P_\infty)\ A_i \tag{8}$$

The lift coefficients can be derived from integrated surface pressure distributions (C_p values). Accordingly, lift coefficients in the present study were estimated by integrating the measured pressure coefficients over the upper surface only. Underbody pressure and shear stress contributions were not included in the calculation. Then the lift coefficient (Cl)is determined using Equation 9 [20], [23].

$$C_l = \frac{F_L}{q\ N} \tag{9}$$

where N is the number of nodes.

Traditional aerodynamic experiments use 6-component force balances to measure lift and drag. However, the UOD wind tunnel does not include a force balance suitable for models of this size and mounting type. As a result, a pressure-based approach was utilised. This method summed the surface pressures distributed over the surface to approximate the aerodynamic stresses. This method is frequently employed in small-scale experimental aerodynamics when force balances are unavailable or incompatible with the model's support structure. A complete uncertainty analysis was conducted to determine the sources of error in the pressure acquisition system, tubing response, manometer resolution, and alignment tolerances. The overall uncertainty in the combined drag and lift forces was determined. We used the uncertainty equations for random and systematic factors to determine the accuracy of the hotwire and digital manometers and the degree of inaccuracy in the measurements. In this case, data were taken from the manufacturer's specifications for pressure taps and hot-wire velocity instruments. For example, Table 3 shows the Testo 425 hot-wire accuracy and the AHJ-501 manometer accuracy at ± 0.3% FSO. hot-wire (speed V): The equation $\Delta V=0.03+0.04V$ applies to speeds V of 20 m/s or less.

Assuming a rectangular distribution, this tolerance can be converted into a standard in velocity reading as stated in equation 10 [28]

$$u_V = \frac{\Delta V}{\sqrt{3}} \tag{10}$$

For a pressure digital manometer, the reading uncertainty can be determined using the following formula.

$$u_P = \frac{\Delta P}{\sqrt{3}} \tag{11}$$

Uncertainty (u) in the pressure distribution above the surface of the car model can be estimated using Equation 12 while accounting for the analytical partial derivative linear propagation in aerodynamics (Equations 5 and 7). [27], [29]

$$u_{Cp,i} = \sqrt{(\frac{1}{q}u_{p,i})^2 + (\frac{-1}{q}u_{p,i})^2 + (\frac{\partial C_{P,i}}{\partial V_{upstream} \cdot u_{Vupstream}})^2} \tag{12}$$

The uncertainty in lift coefficient contribution is as follows

$$CL_i = \frac{C_{P,i}A_i}{A_f} \tag{13}$$

$$u_{CL,i} = \frac{A_i}{A_f}u_{Cp,i} \tag{14}$$

Blockage corrections were applied to both integral aerodynamic coefficients (drag and lift) prior to comparison with free-stream reference data. A first-order empirical correction of the form

$$Cl_{corrected} = \frac{Cl_{\ measured}}{1 + kB} \tag{15}$$

And the uncertainty in the drag coefficient can be calculated using Mercker[16] approach as:

$$Cd_{corrected} = \frac{Cd_{\ measured}}{1 + kB} \tag{16}$$

where B is the blockage ratio and k is the shape parameter of the bluff vehicle. For the present vehicle-type models, k was set to 1.0 (conservative first-order approximation). The same correction form was therefore applied to; Uncertainty introduced by the blockage correction was included in the overall uncertainty budget via RSS propagation (see §3.4).

2.3. Model Validation

To ensure the experimental models adequately depict aerodynamic behaviour and can be relied on to assess aerodynamic performance, validation is an essential first step. Three scaled vehicle models, two based on current commercial cars (Cars 1 and 2) and a newly suggested design (Car 3), were subjected to wind tunnel tests in this study. There is no precise drag coefficient data for the Suzuki Vitara JX 3-door Hard Top (Car 1) or Lamborghini Aventador LP 750-4 (Car 2). A validation of the two cars measured drag features, which are contrasted with published ranges for similar shapes found in Hucho's [23]. C_l values were in a reasonable range (0.28-0.36 for fastbacks, 0.32-0.45 squarebacks). Surface pressure distributions certified the anticipated stagnation, separation and recovery patterns as established in the published literature, representing model fidelity aerodynamically.

The overall aim was to evaluate the effect of shape changes on aerodynamics, i.e., drag, with a special look at how the drag coefficient (C_D) changes with Reynolds number (Re) for three different car shapes. Three diverse car models were looked at, production-type cars, Cars 1 and 2 and a brand-new model, Car 3, schematically represented in Figure 5. Following the obtained results, both Cars 1 and 2's models signify actual vehicle experience at least for the drag coefficient and as Re increased, so does C_D. While comparison between Cars 2 and 3 shows similar C_D behaviour, their differences are not inconsequential; Car 3 has a lower C_D than Cars 1 and 2 especially at high Re. The data proposes that the geometric design changes of Car 3 produce less aerodynamic drag than the previous two designs. If scaled up, the aerodynamic drag on Car 3 would be expected to be less than that of Cars 1 and 2 at the same Reynolds number, thus demonstrating that Car 3 can be used without penalties in real-world driving conditions with enhanced aerodynamics.

There is progressively a disparity between the aerodynamics of different vehicle models as Re decrease. This is chiefly due to the impacts of growing flow separation of the vehicle models and viscous impacts that further intensify the effect of geometrical details of the vehicle. As the Re increases, the benefits of the streamlined shape of the vehicle model become strong when contrasting the aerodynamics of Car 3 with those of the other vehicles. The findings support the request for further experimental investigations to quantitatively evaluate vehicle geometry using validated experimental techniques, and will be valuable to develop the basis for future developments in the design of vehicle aerodynamics. The examinations comprised how the drag coefficient varied as a function of Re to assess aerodynamically accurate scaled models. Figure 5 shows the change in C_D from the effect of changing the Re for all tested configurations. It can be stated that as the Re increases, the C_D decreases. At high Re , the curve for Cd starts to act asymptotically. While the Re range

tested (1.5×10^5–6.0×10^5) does not reach vehicle full-scale (Re >10^7), the behavior of the variables is in agreement with experimental literature on the aerodynamics of scaled models of ground vehicles and appears to be appropriate in appraising trends in aerodynamics and for establishing aerodynamics validation through comparison. Matching of Re to the fifth degree and constituency would be the original way to contrast editions of these (different) sized geometry models that are similar in structure. Only by using a common numerator of aerodynamic coefficients (at or near equal Re), the question is whether it is possible to keep the effect of viscous versus inertial forces equal from one configuration to another. This method is widely used to deliver a means of making appropriate 'comparisons' between different vehicles' aerodynamic performances, when an exact geometric analogy is not sustainable.

The literature data provided in Table 6 signifies the experimental range of 'simplified' passenger vehicle geometries (tested in a wind tunnel) at comparable Re approximately 10 to 20 times greater than obtained in the present study (105-106). The present study values can be found in 'Drag' and Lift coefficients; using each vehicle Type's (Car 1, Car 2 and so on) data is based on corrected Drag/lift coefficients from present measurements. The findings demonstrated in Table 6 (Geometric Corrections) support that the present study's results for the types of vehicles characterized are in accordance with the results found in the laboratory tests performed on the same types, using test equipment specified in this study. The Car 1 Vehicle is a Traditional (Squareback); Car 2 Vehicle is 'Fastback' and the Car 3 Vehicle is 'Fastback' design based on Car 2 with/without Rear Wing.

For Car 1 (squareback design), C_D decreased from C_D = 0.385 at a low Re ($Re \approx 1.52\times105$) to a C_D = 0.344 at a high Re ($Re \approx 5.34\times105$). Lift coefficient (C_l) also decreased over this same range from C_l = 0.423 to C_l = 0.204. The trends and magnitudes observed for the two test configurations are consistent with those reported for squareback and Ahmed-type vehicles. For Car 2 (fastback), the corrected C_D decreased from C_D = 0.292 at low Re to C_D = 0.247 at high Re, while the lift coefficient decreased from C_l = 0.658 to C_l = 0.285. Both the C_D and C_l values for the fastback configuration are consistent with values found for fastback automobiles in the literature confirming the expected sensitivity of streamlined rear-end designs to the Re.

Table 6. Comparison of corrected C_D and C_l values with literature data [19], [23], [30], [31]

Vehicle type	Reynolds number	C_D (Literature)	C_l (Literature)	C_D(Present study)	C_l(Present study)
Car 1	Low Re (≈1.5×105)	0.36–0.42	0.25–0.45	0.385	0.423
	Mid Re (≈2.9×105)	0.34–0.40	0.18–0.35	0.372	0.300
	High Re (≈5.3×105)	0.32–0.38	0.10–0.25	0.344	0.204
Car 2	Low Re (≈1.5×105)	0.30–0.36	0.45–0.70	0.292	0.658
	Mid Re (≈2.9×105)	0.28–0.34	0.30–0.55	0.274	0.436
	High Re (≈5.3×105)	0.26–0.32	0.20–0.40	0.247	0.285
Car 3	Low Re (≈1.5×105)	0.26–0.32	0.60–0.90	0.272	0.813
	Mid Re (≈2.9×105)	0.25–0.30	0.35–0.60	0.265	0.455
	High Re (≈5.3×105)	0.23–0.28	0.10–0.30	0.242	0.161
Car 3 (with rear wing)	Low Re (≈1.5×105)	0.27–0.33	0.40–0.65	0.297	0.610
	Mid Re (≈2.9×105)	0.26–0.32	0.25–0.45	0.283	0.350
	High Re (≈5.3×105)	0.25–0.31	0.05–0.20	0.262	0.120

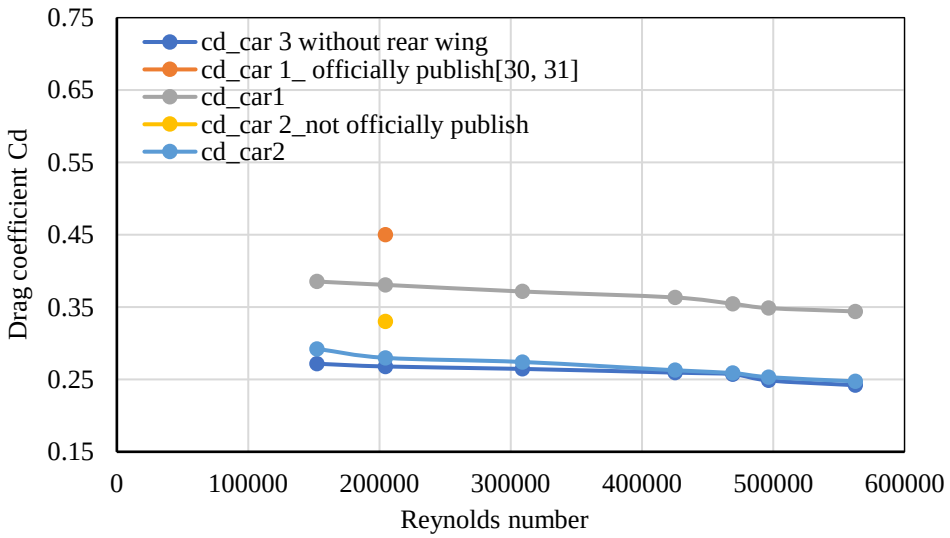

Figure 5 The corrected drag coefficient trends as a function of Reynolds number for Cars 1–3, along with a comparison with published experimental data [30],[31]

Car 3 (fastback, inspired by Car 2) has the lowest baseline value in any of the configurations tested. Similar to Car 2, as Re increases for Car 3, the C_D decreases from C_D = 0.272 to C_D = 0.242. Without a rear wing, however, Car 3 data show relatively large amounts of positive lift at low Re (C_l = 0.813) that have been observed to drop rapidly to C_l = 0.161 as Re is increased. Similar findings for the fastback configuration can be found in the SAE technical papers and review texts. When a rear wing is added to Car 3, the drag coefficient increases moderately, from C_D = 0.297 at low Re to C_D = 0.262 at high Re, while the lift coefficient is substantially reduced from C_l = 0.610 to C_l = 0.120. This confirms that the rear wing effectively suppresses lift with only a limited drag penalty, in close agreement with published experimental findings on winged fastback vehicles. Overall, the Reynolds-number dependence and absolute magnitudes of C_D and C_l obtained in the present study are consistent with authoritative literature sources, providing strong validation of the experimental methodology and correction procedures used in this work.

3. Results and Discussion

3.1 Ground Effect and Boundary-Layer Influence

To justify the validity of the measurements, a quantitative assessment of the wind-tunnel floor boundary-layer thickness was performed. At the highest Reynolds number tested, the estimated boundary-layer thickness was $\delta \approx 6$–8 mm. For Car 2 and Car 3, this corresponds to less than 14% of the effective model ride height, which is within the acceptable range reported in small-scale ground-vehicle wind-tunnel studies. Consequently, although the stationary floor condition affects the underbody flow, its influence is systematic and comparable across all tested configurations, allowing reliable relative comparisons of aerodynamic coefficients. The implications of this limitation on underbody flow development and the absolute magnitude of lift and drag are therefore acknowledged.

3.2 Pressure Coefficient Distribution

The investigation began by analysing the fluid dynamics surrounding a static, fundamental automotive architecture. These results were the standards. Then, a rear wing was put on Car 3. The purpose of the study was to examine how adding movable aerodynamic parts affected the body's aerodynamic qualities and compare them to those of Cars 1 and 2, which had shapes that looked authentic. The investigation of the flow area near the vehicle yields the drag and lift coefficients, the distribution of pressure coefficient C_p values throughout the automobile's surface at various Re, and the local velocity distribution along the vehicle's surface. Figures 6 (a and b) illustrate how the pressure coefficient C_p changes along the surface of a basic automobile model for different Re. Figures 6 (a and b) show how the pressure coefficient (C_p) changes along the longitudinal centerline of the upper surfaces of Car 1 and Car 2 at varying Re. Just downstream of the stagnation point, close to the leading edge of the hood, we observe a reduction in pressure. This indicates that the flow is accelerating and beginning to split.

A change in the shape of the pressure recovery causes a peak in C_p at the hood–windscreen junction. A pressure drops over the transition from the windscreen to the roof further downstream implies that the flow is speeding up and that the system is more likely to become unstable. C_p slowly rises towards the back window and trunk area, indicating that some of the flow is reattached and the pressure is recovered on the upper back surface. Overall, the distribution shows typical aerodynamic properties, including stagnation, separation, and recovery, that are in line with what Hucho [23] found for road cars, even though the shapes of the vehicles are different. These results show that surface pressure is sensitive to changes in geometry and back up the accuracy of the measured pressure distribution for the current model.

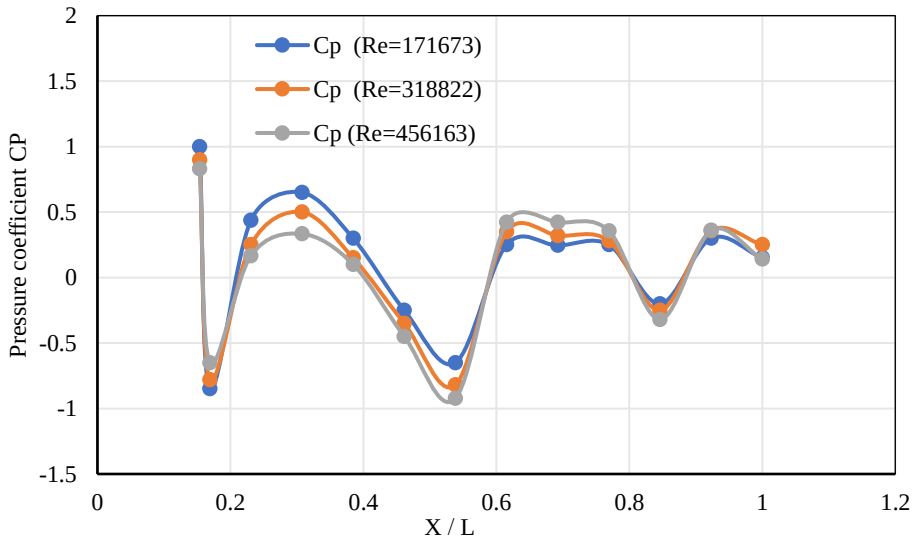

Figure 6.a. Distribution of the pressure coefficient C_p values along the Car 1 model at different Re

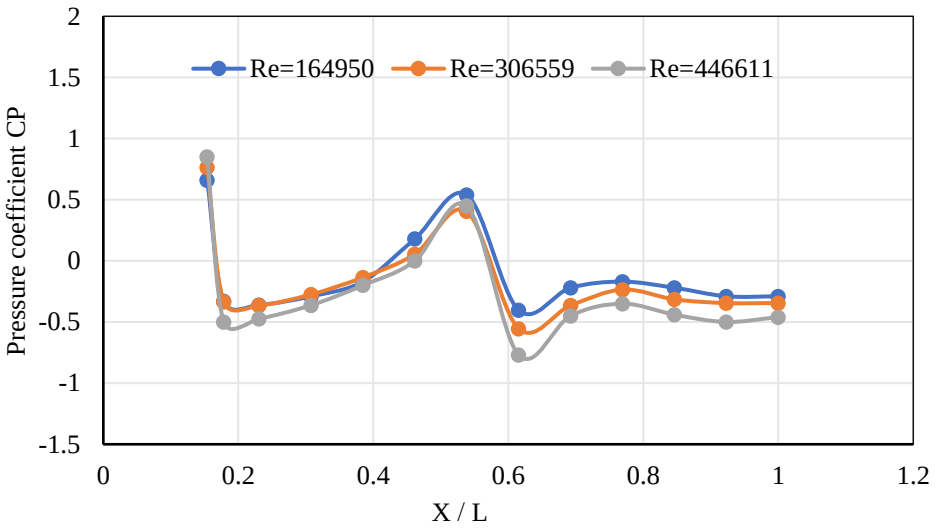

Figure 6.b. Distribution of the pressure coefficient C_p values along the Car 2 model at different Re

3.3 Local Velocity Distribution

Based on the data, the air velocity increased considerably in areas of curvature with convexity, consistent with the decrease in pressure predicted by Bernoulli's principle. Higher Re leads to thinner boundary layers, delaying boundary layer separation and thus resulting in lower drag forces (particularly with respect to Car 2). Also, due to the squareback "cubit" geometry of Car 1, it had the largest wake and lowest rear-end air velocity measurements and proved to have a greater drag than Car 2. Figures 7 (a and b) show the local surface velocity distributions for both the Car 1 and Car 2 wind tunnel models at two different Re. At the higher Re (4.56 x 10^5), the peak surface velocities are greater than those at a lower Re (1.71x10^5), with the exception of the areas with curvature, which caused accelerating flow velocities from having less of a shear layer and less of a viscous influence affecting the flow field across the entire model. Conversely, the velocity distribution at the lower Re is more consistent with lower peak surface velocity than the higher Re is due to a thicker boundary layer with the increased effects of shear and viscous forces that could lead to an increase in pressure drag. Understanding this behaviour is important when applying results from wind tunnel testing to real-world, full-size vehicle applications, whether using wind tunnel-derived or computationally derived data. Even though there is no ability to do full flow field visualization from any of the measurement techniques being used, the data indicate that each of the measurement techniques does work together to provide an indirect, but physically consistent picture of the wake structure and the separation that occurs. The trend in Cp recovery and region of downstream velocity deficits correspond closely with the observed drops in Drag Coefficient, supporting an aerodynamic explanation.

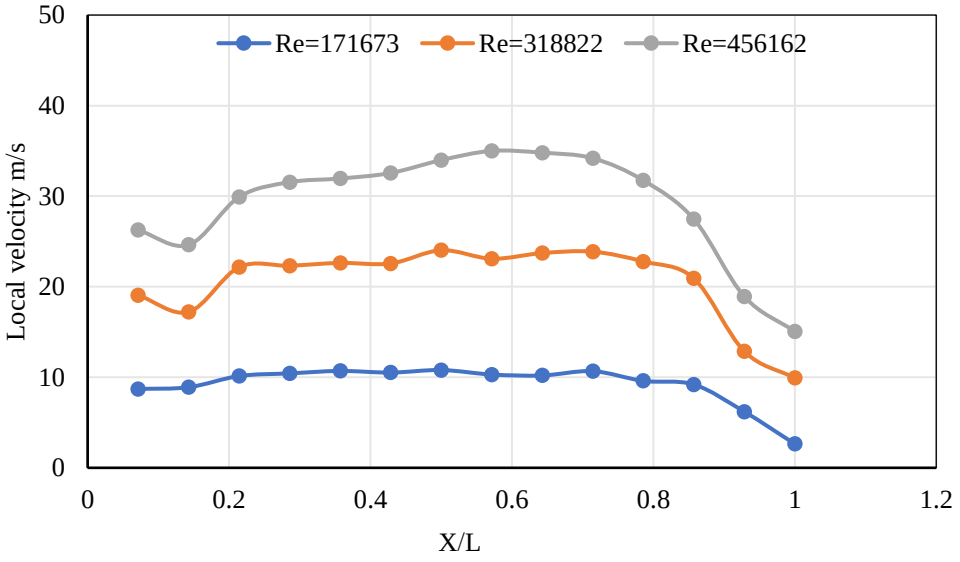

Figure 7.a. Distribution of the local velocity values along the Car 1 model for different Re

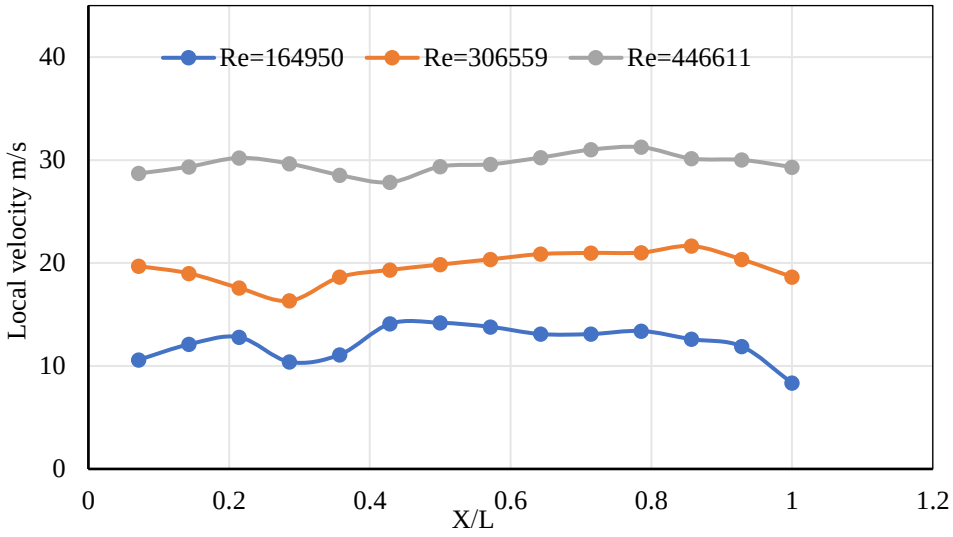

Figure 7.b. Distribution of the local velocity along the Car 2 model for different Re

3.4. Effect of Rear Wing on Car 3

3.4.1 Pressure coefficient distribution

The distribution of pressure coefficient (C_p) along the midline of Car 3 at different Re without (baseline) and with (W) a rear wing at 411264 Re is illustrated. Results of Figure 8 indicate that a rear wing has a major effect on the aft pressure field, so that the C_p is lower and, therefore, creates more suction and produces greater downforce, with this effect becoming increasingly pronounced Re increases from 154776 to 411264. Additionally, as inertial forces dominate at higher Re and because of greater sensitivity of flow to geometry change, the C_p gradient is more uniform and pressure recovery is slower (by 18% at the front and by 171% at the rear) when using a rear wing, which indicates better flow attachment and less flow separation, which corresponds to improved aerodynamic efficiency. Finally, supporting Hucho's findings [23] regarding the Audi 100III, these results support the important role of rear aerodynamic devices in affecting the pressure field, and the effectiveness of these devices increases with Re.

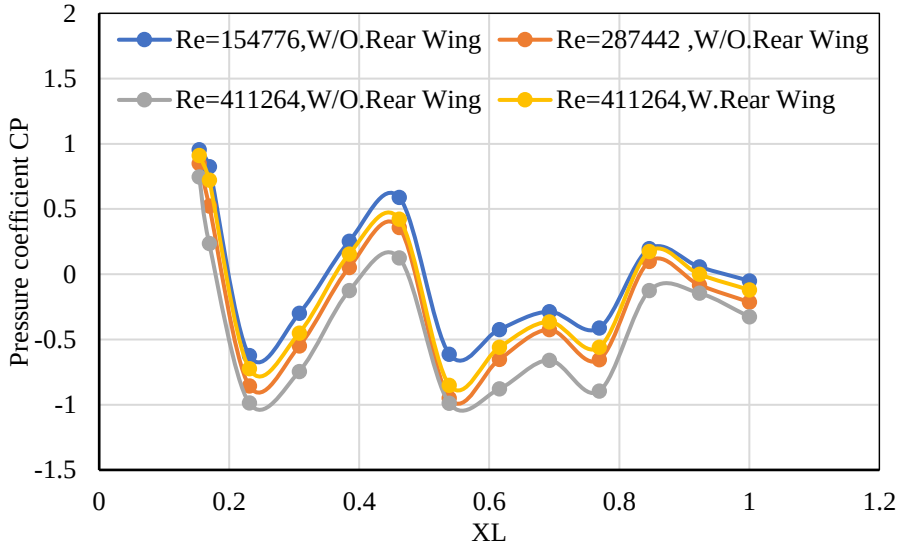

Figure 8. Pressure coefficient (C_p) distribution along the Car 3, both with and without the addition of a rear wing at variable Re

3.4.2 Drag coefficient comparison

A comparison of C_D for the drag coefficients (C_D) of Car 3 with and without a rear wing over different Re is shown in Figure 9 and illustrates how the drag coefficient changes with varying flow conditions. At low Re, C_D = 0.242 for no rear wing and C_D = 0.261 for the rear wing. The rear wing configuration represents a 7.9% increase in total drag due to increased wake turbulence and greater flow separation, which are typically found in low-Re, viscosity-dominated conditions. Also, the drag coefficient for the rear wing configuration is lower than that reported by Hucho [23] for the Volkswagen 1600 rear spoiler configuration. However, the drag coefficient difference diminishes with increased Re, indicating that as the Re increases, the aerodynamic penalties associated with the rear wing configuration become less

significant and could potentially result from more favourable wake dynamics or more efficient flow reattachment at higher speeds. These results highlight the importance of conducting Re-scaled tests, as aerodynamic devices that appear to create undesirable characteristics at model scale may perform more favourably at full-scale conditions.

Error bars represent the combined experimental uncertainty of the corrected drag coefficient (± 0.63% for Car 2; ± 0.67% for Car 3, and ± 1.27 % for Car 1) and the corrected lift coefficient (± 0.57% for Car 2; ± 0.92% for Car 3, and ± 0.42 % for Car 1), including contributions from instrumentation, blockage corrections, geometric deviations, and surface roughness. The observed change in drag coefficient due to the rear wing is less than the associated uncertainty (≤ 0.9%), indicating that the wing-induced drag variation is physically meaningful rather than a result of measurement scatter. The overall corrected drag and lift coefficients, along with their uncertainties for all configurations, are summarised in Table 7. Car 3 had the lowest C_D across the Reynolds number range studied. It had a maximum decrease of almost 29% compared to Car 1 and a small improvement compared to Car 2. This decrease in drag is due to improved rear-end pressure recovery and a smaller wake velocity disadvantage. The reported 26% decrease in the drag coefficient is based on integral aerodynamic coefficients corrected for obstruction. This is backed up by a full uncertainty analysis showing that the improvement is greater than the combined experimental uncertainty.The drag coefficient goes down as the Re goes up because the boundary layer gets thinner and flow separation happens later as inertial processes take over. At higher Re, the drag trends show less susceptibility to changes in Re. This suggests that the behaviour is approaching independence from Re within the investigated range. This behaviour aligns with traditional aerodynamic studies of road vehicles, which indicate that Re independence is attained gradually rather than suddenly, especially in bluff-body configurations.

Table 7. Corrected drag and lift coefficients and their uncertainties for Cars 1–3 at different Re

Configuration	Re	$C_D \pm \Delta\,(C_D)$	$C_l \pm \Delta\,(C_l)$
Car 1	Low Re (≈1.52×10⁵)	0.3853 ± 0.01429	0.42288 ± 0.008711
	Mid Re (≈2.9×10⁵)	0.3715 ± 0.01378	0.2997 ± 0.00617
	High Re (≈5.34×10⁵)	0.3440 ± 0.01276	0.20402± 0.004202
Car 2	Low Re (≈1.52×10⁵)	0.2922 ± 0.00812	0.65768 ± 0.01335
	Mid Re (≈2.9×10⁵)	0.2741 ± 0.007621	0.43601 ± 0.00885
	High Re (≈5.34×10⁵)	0.2472 ± 0.006346	0.2845 ± 0.00577
Car 3 (without wing)	Low Re (≈1.52×10⁵)	0.2717 ± 0.00755	0.81338 ± 0.0187
	Mid Re (≈2.9×10⁵)	0.2645 ± 0.00735	0.45501 ± 0.009211
	High Re (≈5.34×10⁵)	0.2420 ± 0.006727	0.1605 ± 0.003693
Car 3 (with wing)	Low Re (≈1.52×10⁵)	0.2970 ± 0.00825	0.61001 ± 0.01403
	Mid Re (≈2.9×10⁵)	0.2832 ± 0.00787	0.35 ± 0.00713
	High Re (≈5.34×10⁵)	0.2619 ± 0.00728	0.12 ± 0.00276

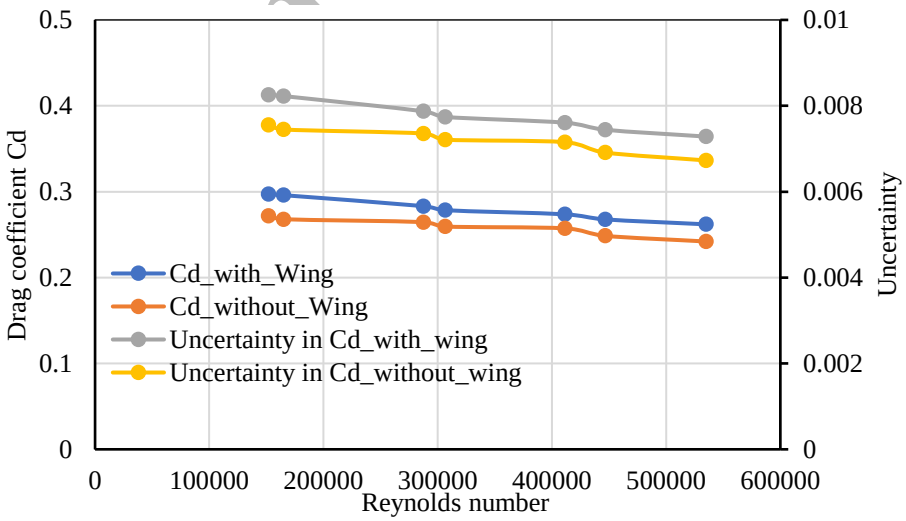

Figure 9. Corrected drag coefficient (C_D) variation with Reynolds number for the Car 3 both with and without a rear wing

3.4.3 Lift coefficient comparison

We aim to determine whether the addition of a rear wing to the car influences the downforce. Figure 10 shows how the corrected lift coefficient (C_l) and Reynolds number (Re) are related. It also shows how adding a rear wing to Car 3 changes these values. It is clear to show that the CL goes down as the Reynolds number goes up. The result means that aerodynamic lift goes down or, in the case of vehicle design, downforce goes up. This decreased lift is a good thing for high-performance cars since more downforce at higher speeds makes the tyres grip better and the car more stable without adding weight. It is clear to show that the C_l goes down as the Reynolds number goes up. This means that aerodynamic

lift goes down or, in the case of vehicle design, downforce goes up. This phenomenon is a good thing for high-performance cars since more downforce at higher speeds makes the tyres grip better and the car more stable without adding weight. The rear wing seems to manage airflow well by making more downforce as speed and Reynolds number go up. This makes the vehicle's aerodynamic profile better. This trend shows that the rear wing on Car 3 works better at higher speeds, which is vital for racing and performance driving. Hucho [23] reports that the C_l of the Volkswagen 1600 with a notchback is 0.18 after adding a rear wing. Our best result at high Re is 0.12. Adding a rear wing to Car 3 reduces the lift coefficient by ~10–20 % over the whole range of Re.

As the Re increases, the corrected amount of downforce reduces further as the wing-induced suction force is greater than before and the rear wake is more stable at that point in time. Thus, it produces a stabilizing effect on the vehicle with greater downforce at higher Re and therefore provides greater grip from the tyres with very little additional drag when at higher Re. Since all lift coefficients (C_l) reported were obtained from integration of pressures measured on the upper surface of the wings, these values are intended to represent only aerodynamic comparisons rather than absolute total vehicle lift. While the absence of pressure measurements beneath the vehicle precludes predicting total lift, the comparison method is valid for assessing overall aerodynamic properties under identical experimental conditions.

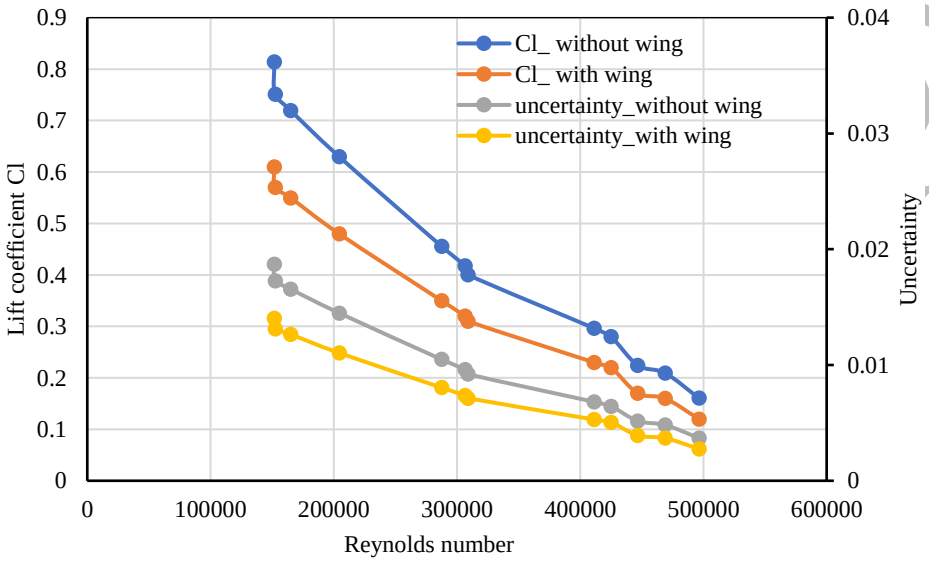

Figure 10. Variation of the corrected lift coefficient (C_l) with Reynolds number for Car 3 with and without a rear wing

4. Conclusion and Future Work

The aerodynamics of three scaled-down (5%) vehicle configurations were examined to assess the effects of Re and the effects of adding a rear wing to Car 3. From the corrected data, the coefficient of drag for all three configurations decreased with Re, indicating a transition from a flow dominated by viscous forces to one dominated by inertial forces. Of the three configurations, Car 3 showed the best baseline aerodynamic performance with a minimum drag coefficient of approximately 0.242 (26% - 2% lower drag than Cars 1 and 2) respectively. The addition of a rear wing on Car 3 made it meaningfully more aerodynamic. At low Re, the rear wing increased the vehicle's drag by a small amount (7.2 %) due to increased wake turbulence. However, as the Re increased, the drag contribution of the rear wing decreased. More importantly, the rear wing consistently reduced Car 3's lift by 12%-18%, with a minimum lift coefficient of 0.12. This value is in close agreement with the lift coefficient of 0.18 reported by Hucho for similar notchback vehicles. The difference in lift attributable to the installation of the rear wing on Car 3 exceeded the experimental uncertainty (± 3.1%), thus representing a true aerodynamic benefit linked to downforce increase. The drag and lift coefficients are consistent with the literature published. The results demonstrate that the blockage correction and measurement techniques are both reliable.

Comparisons of the CAD models to the 3D-printed models showed less than 0.7% differences in geometry, which are equivalent to less than 1% of total aerodynamic uncertainty. Generally, these findings validate that small wind-tunnel tests with suitable correction methodology can produce accurate and significant information on the aerodynamic performance of vehicles. Accordingly, the results suggest that improved rear geometry and rear wings can contribute to improved high-speed stability. Future studies should systematically measure yaw-angle and crosswind effects, use a moving ground and rotating wheels to measure underbody flow, utilise PIV to measure flow and integrate test data with numerical optimisation frameworks to enhance absolute aerodynamic force forecasting accuracy.

Acknowledgments

The author would like to express his heartfelt appreciation to the Department of Mechanical Engineering, University of Diyala, for their continual support and help in using the wind tunnel (WT) facility. We would like to thank Dr. Nazar M. Aldabash, Dr. Mudhar A. Al-Obaidi and Dr. Itimad D. J. Azzawi for their helpful support in developing one of the car models that were utilized in this study. The author also warmly recognizes Engineers Hind J. and Mustafa A. for their

excellent technical support and efforts in this work. The author would like to thank also the Manchester International Training Academy (MINTA), United Kingdom, and Prof. Dr. Eng. Abdul Salam Darwish for providing excellent English proofreading and linguistic editing services for the paper.

Funding
This research received no external funding.

Declaration of Competing Interest
The author declares no conflicts of interest.

CRediT Authorship Contribution Statement
Mohammed Kh. Abbas (Methodology; Validation; Formal analysis; Data curation; Formal analysis; Investigation; Resources; Software; Visualisation; Writing - original draft; Writing - review & editing; Funding acquisition; Project administration, Revised, and approved the final version of the manuscript)

Availability of Data and Materials
The author confirms that the data that support the findings of this study are available within the article.

Ethics Statement
This study did not involve human participants or animal subjects. Therefore, ethical approval was not required for this research.

Generative Artificial Intelligence Declarations
The authors report that generative artificial intelligence (AI) techniques were not used in the creation of the scientific content, concepts, analysis, or findings given in this study. Any AI-assisted technologies employed were only used for the purpose of language improvement and readability enhancement under stringent human oversight and control. The authors are responsible for the integrity, accuracy and final content of the paper.

Nomenclature

Symbols	Description	Symbols	Description
A_f	The frontal area of the scale model [mm2]	$V_{downstream}$	The downstream velocity[m/s]
A_w	The area of the wind tunnel section [mm2]	$V_{upstream}$	The upstream velocity[m/s]
B	The blockage ratio [-]	q	The dynamic pressure [Pa]
C_D	Drag coefficient [-]	P_∞	static pressure [Pa]
C_l	Lift coefficient [-]	P_i	local surface pressure [Pa]
C_p	Pressure coefficient [-]	Re	Reynolds number [-]
F_L	The lift force [N]	ρ	The air density [kg/ m3]
$F_{d_{act}}$	An actual drag force [N]	u_V	The uncertainty in velocity reading
$F_{d_{the}}$	The theoretical drag force [N]	u_P	The uncertainty in pressure reading
k	The shape parameter of the vehicle [-]	SUV	sports utility vehicle

References

[1] B. Junaidin, "Aerodynamic analysis of sport utility vehicle (SUV) by computational fluid dynamics (CFD) approach," *Vortex*, vol. 3, no. 1, p. 67, 2022. https://doi.org/10.28989/vortex.v3i1.1161

[2] D. Dhande, M. Bauskar, "Analysis of aerodynamic aspects of SUV by analytical and experimental method," *International Journal of Emerging Technology and Advanced Engineering*, vol. 7, pp. 447-451, 2008.

[3] G. Bonnavion, J. Borée, V. Herbert, "On the use of kinetic energy balance for the volumetric identifications of drag sources of a blunt body. Application to road vehicles," *International Journal of Heat and Fluid Flow*, vol. 96, p. 108977, 2022. https://doi.org/10.1016/j.ijheatfluidflow.2022.108977

[4] M. Mohammadi, S.M.R. Nazemosadat, D. Fazel, Y.B. Lari, "An integrated approach for structural modeling, modal analysis, and aerodynamic evaluation of an electric vehicle body shell using finite element method and computational fluid dynamics," *Materials Today Communications*, vol. 45, p. 112331, 2025. https://doi.org/10.1016/j.mtcomm.2025.112331

[5] A. Al-Saadi, K. Al-Farhany, K.K. Idan Al-Chlaihawi, W. Jamshed, M.R. Eid, E.S.M. Tag El Din et al., "Improvement of the aerodynamic behavior of a sport utility vehicle numerically by using some modifications and aerodynamic devices," *Journal of Scientific Reports*, vol. 12, no. 1, p. 20272, 2022. https://doi.org/10.1038/s41598-022-24328-w

[6] D. Ramasamy, K. Mohanesan, K. Kadirgama, M.M. Noor, M.M. Rahman, "Hybrid electric vehicle car body drag analysis using computational fluid dynamics," *International Journal of Automotive and Mechanical Engineering*, vol. 14, no. 3, pp. 4496–4507, 2017. https://doi.org/10.15282/ijame.14.3.2017.8.0355

[7] P. Qin, A. Ricci, B. Blocken, "CFD simulation of aerodynamic forces on the DrivAer car model: Impact of computational parameters," *Journal of Wind Engineering and Industrial Aerodynamics*, vol. 248, p. 105711, 2024. https://doi.org/10.1016/j.jweia.2024.105711
[8] Y. Gan, L. Li, "Optimization of aerodynamic profile of ground vehicle," in *Journal of Physics: Conference Series*, Institute of Physics, vol. 2569, no. 1, p. 012068, 2023. https://doi.org/10.1088/1742-6596/2569/1/012068
[9] M. Syafiq, I.A. Ishak, M. Arafat, R. Abd Rashid, N.E. Othman, Z.M. Salleh et al., "Computational fluid dynamics analysis of aerodynamic characteristics on overtaking vehicles in crosswind conditions," *International Journal of Automotive and Mechanical Engineering*, vol. 22, no. 2, pp. 12373–12387, 2025. https://doi.org/10.15282/ijame.22.2.2025.10.0947
[10] X. Liang, X. Gao, T. Gu, X. Jia, "Aerodynamic drag coefficient analysis of heavy-duty vehicle platoons: A hybrid approach integrating wind tunnel experiments and CFD simulations," *Energies (Basel)*, vol. 17, no. 24, p. 6383, 2024. https://doi.org/10.3390/en17246383
[11] S. Rajendran, I.A. Ishak, M. Arafat, A.F. Mohammad, Z.M. Salleh, N.A. Samiran, M.N.M. Ja'at et al., "Aerodynamic effects of high-speed train positions during tunnel exit under crosswind conditions using computational fluid dynamics," *International Journal of Automotive and Mechanical Engineering*, vol. 21, no. 2, pp. 11191–11202, 2024. https://doi.org/10.15282/ijame.21.2.2024.2.0865
[12] Yunus A. Çengel and John M. Cimbala, Fluid Mechanics: Fundamentals and Applications, —1st ed. Published by McGraw-Hill, a business unit of The McGraw-Hill Companies, Inc., 2006.
[13] J. J. Cerutti, G. Cafiero, and G. Iuso, "Aerodynamic drag reduction by means of platooning configurations of light commercial vehicles: A flow field analysis," *International Journal of Heat and Fluid Flow*, vol. 90, Aug. 2021, https://doi.org/10.1016/j.ijheatfluidflow.2021.108823
[14] A. W. Huluka and C. H. Kim, "Effect of the air duct system of a simplified vehicle model on aerodynamic performance," *International Journal of Automotive and Mechanical Engineering*, vol. 17, no. 2, pp. 7985–7995, Apr. 2020. https://doi.org/10.15282/ijame.17.2.2020.17.0598
[15] M. K. Abbas, N. M. Aldabash, Y. A. J. Almahdawi, I. D. J. Azzawi, and M. A. Al-Obaidi, "Synergistic experimental-numerical study for assessing the aerodynamic performance of a simplified road vehicle," *Advances in Science and Technology Research Journal*, vol. 20, no. 5, pp. 322–334, May 2026, doi: 10.12913/22998624/215653
[16] E. Mercker, "A blockage correction for automotive testing in a wind tunnel with closed test section," *Journal of Wind Engineering and Industrial Aerodynamics*, vol. 22, pp. 149–167, 1986.
[17] C. Zhang, J. Chen, J. Zhao, X. Wu, "Research on model validation and uncertainty quantification of airfoil flow," in *Journal of Physics: Conference Series*, IOP Publishing Ltd, vol. 1985, no. 1, p. 012015, 2021. https://doi.org/10.1088/1742-6596/1985/1/012015
[18] Z. Deng, S. Yu, C. Wu, "Numerical simulation and analysis for aerodynamic devices of FSAE racing car," in *Journal of Physics: Conference Series*, Institute of Physics Publishing, vol. 1600, no. 1, p. 012079, 2020. https://doi.org/10.1088/1742-6596/1600/1/012079
[19] A. Şumnu, Y. Eraslan, "Aerodynamic shape optimization of simplified ground vehicle (Ahmed Body) using passive control devices," *Mechanika*, vol. 31, no. 1, pp. 5–14, 2025, https://doi.org/10.5755/j02.mech.36452
[20] M.S. Abood, I.Y. Hussain, A.H. Ali, "A theoretical and experimental investigation of the effects of inverted wings modifications on the stability and aerodynamic performance of a sedan car at cornering," *Engineering Reports*, vol. 7, no. 1, p. e13026, 2025. https://doi.org/10.1002/eng2.13026
[21] Y. A. Almahdawi, M. K. Abbas, N. Aldabash, "Temperature effect in the energy degradation of photovoltaic power Temperature effect in the energy degradation of photovoltaic power," *Journal of Thermal Engineering*, vol. 9, no. 5, pp. 1153–1162, 2023. https://doi.org/10.18186/thermal.00000
[22] A. Al-Saadi, K. Al-Farhany, A.E. Faisal, M.A. Alomari, W. Jamshed, M.R. Eid et al., "Improvement of the aerodynamic behaviour of the passenger car by using a combine of ditch and base bleed," *Journal of Scientific Reports*, vol. 12, no. 1, p. 18462, 2022. https://doi.org/10.1038/s41598-022-23183-z
[23] W.-Heinrich. Hucho, Aerodynamics of road vehicles: from fluid mechanics to vehicle engineering. Butterworth-Heinemann, 1987.
[24] P. Chauhan, M. Ja'fari, A.J. Jaworski, "A numerical study of horizonal axis wind turbine blade Contamination: Aerodynamic and sustainable impacts," *Renewable Energy*, vol. 256, p. 124033, 2026. https://doi.org/10.1016/j.renene.2025.124033
[25] P. Bulat, P. Chernyshov, N. Prodan, K. Volkov, "Control of aerodynamic characteristics of thick airfoils at low reynolds numbers using methods of boundary layer control," *Fluids*, vol. 9, no. 1, p. 26, 2024. https://doi.org/10.3390/fluids9010026
[26] K. Rogowski, R.F. Mikkelsen, J. Michna, J. Wiśniewski, "Aerodynamic performance analysis of NACA 0018 airfoil at low Reynolds numbers in a low-turbulence wind tunnel," *Advances in Science and Technology Research Journal*, vol. 19, no. 2, pp. 136–150, 2025. https://doi.org/10.12913/22998624/195556
[27] N. Kubo, S. Bhandari, M. Tanaka, T. Nonomura, H. Kawabata, "Experimental parametric study on flow separation control mechanisms around NACA0015 airfoil using a plasma actuator with burst actuation over Reynolds numbers of 105–106," *Applied Sciences* (Switzerland), vol. 14, no. 11, p. 4652, 2024. https://doi.org/10.3390/app14114652
[28] X. Peng, H. Zhu, D. Xu, M. Xiao, W. Wang, G. Cai, "Aerodynamic performance uncertainty analysis and optimization of a conventional axisymmetric vehicle based on parallel polynomial chaos expansions," *Aerospace*, vol. 9, no. 8, p. 396, 2022. https://doi.org/10.3390/aerospace9080396

[29] S.N. Leloudas, A.I. Eskantar, G.N. Lygidakis, I.K. Nikolos, "Low Reynolds airfoil family for small horizontal axis wind turbines based on RG15 airfoil," *SN Applied Sciences*, vol. 2, no. 3, p. 371, 2020. https://doi.org/10.1007/s42452-020-2161-1
[30] Motor Matchup, "2000 Suzuki Vitara JLX 2.0 2DR 4X4 — 127 HP, 0-60 in 10.2s," *Motor Matchup*. [Online]. Available: https://www.motormatchup.com/catalog/Suzuki/Vitara/2000/JLX-2.0-2DR-4X4
[31] CarSpecs.us, "1999 Suzuki Vitara," [Online]. Available: https://www.carspecs.us/cars/1999/suzuki/vitara/7927